Acta Med. Okayama, 2023
Vol. 77, No. 3, pp. 273-280

Acta Medica Okayama
http://escholarship.lib.okayama-u.ac.jp/amo/

Original Article

Usefulness of Simple Diffusion Kurtosis Imaging for Head and Neck Tumors: An Early Clinical Study

Yudai Shimizu[a§], Masahiro Kuroda[b*§], Yuki Nakamitsu[b§], Wlla E. Al-Hammad[a], Suzuka Yoshida[a], Yuka Fukumura[a], Yoshihide Nakamura[a], Kazuhiro Kuroda[b,c], Ryo Kamizaki[b], Satoshi Imajoh[b], Yoshinori Tanabe[b], Kohei Sugimoto[d], Masataka Oita[d], Irfan Sugianto[e], Babatunde O. Bamgbose[f], Yoshinobu Yanagi[g], and Junichi Asaumi[h]

[a]Department of Oral and Maxillofacial Radiology, Okayama University Graduate School of Medicine, Dentistry and Pharmaceutical Sciences, [b]Radiological Technology, Graduate School of Health Sciences, Okayama University, Departments of [g]Dental Informatics, [h]Oral and Maxillofacial Radiology, Faculty of Medicine, Dentistry and Pharmaceutical Sciences, [d]Graduate School of Interdisciplinary Sciences and Engineering in Health Systems, Okayama University, Okayama 700-8558, Japan, [c]Department of Health and Welfare Science, Graduate School of Health and Welfare Science, Okayama Prefectural University, Okayama 719-1197, Japan, [e]Department of Oral Radiology, Faculty of Dentistry, Hasanuddin University, Makassar, Sulawesi 90245, Indonesia, [f]Department of Oral Diagnostic Sciences, Faculty of Dentistry, Bayero University, Kano 00234, Nigeria.

Diffusion kurtosis (DK) imaging (DKI), a type of restricted diffusion-weighted imaging, has been reported to be useful for tumor diagnoses in clinical studies. We developed a software program to simultaneously create DK images with apparent diffusion coefficient (ADC) maps and conducted an initial clinical study. Multi-shot echo-planar diffusion-weighted images were obtained at b-values of 0, 400, and 800 sec/mm^2 for simple DKI, and DK images were created simultaneously with the ADC map. The usefulness of the DK image and ADC map was evaluated using a pixel analysis of all pixels and a median analysis of the pixels of each case. Tumor and normal tissues differed significantly in both pixel and median analyses. In the pixel analysis, the area under the curve was 0.64 for the mean kurtosis (MK) value and 0.77 for the ADC value. In the median analysis, the MK value was 0.74, and the ADC value was 0.75. The MK and ADC values correlated moderately in the pixel analysis and strongly in the median analysis. Our simple DKI system created DK images simultaneously with ADC maps, and the obtained MK and ADC values were useful for differentiating head and neck tumors from normal tissue.

Key words: simple diffusion kurtosis imaging, mean kurtosis, clinical trial, head and neck tumor, magnetic resonance imaging

Magnetic resonance imaging (MRI) shows a higher resolution of soft tissues than computed tomography (CT). MRI, particularly diffusion-weighted (DW) imaging (DWI), is increasingly being used in clinical practice to diagnose tumors [1-3].

Although apparent diffusion coefficient (ADC) values are calculated using DWI, ADC maps are now widely used in routine clinical practice. The potential usefulness of restricted diffusion-weighted (RD) imaging (RDI) [4,5] is being investigated. RDI demonstrates the degree to which the movement of water molecules is restricted by membrane structures and other factors within tissues. RDI, including diffusion kurtosis (DK) imaging (DKI) and Q-space imaging, is

Received November 6, 2022; accepted December 5, 2022.
*Corresponding author. Phone: +81-86-235-6873; Fax: +81-86-235-6873
E-mail: kurodamd@cc.okayama-u.ac.jp (M. Kuroda)
[§]These authors contributed equally to this work.

Conflict of Interest Disclosures: No potential conflict of interest relevant to this article was reported.

also being clinically investigated [6, 7] in clinical studies.

DKI involves numerous b-values in 30 axes and a high maximum b-value, increasing the imaging time [8-10]. Moreover, the software to create DK images is not widely available in daily clinical practice. Therefore, DKI has not progressed from clinical research to routine clinical practice.

A software program and fast DKI method have been developed to overcome these shortcomings of DKI [11, 12]. Hamada *et al.* developed a program that could be used universally in clinical practice and also reported an easy method for creating RD images [11]. Regarding the high maximum b-value, since imaging of head and neck tumors requires shorter imaging time to avoid body movement and reduce image distortion, and since tissues in the head and neck are almost isotropic and have little restricted diffusion, Kuroda *et al.* attempted to decrease the maximum b-value and create DKI using the triple-axis DW images used in daily clinical practice [12]. Their fast DKI method uses a low maximum b-value and a readout segmentation of long variable echo-train sequences (RESOLVE) with a 3-scan trace for DW images acquired when creating ADC maps in routine clinical practice to acquire DK images and ADC maps simultaneously. The imaging method [12] in which DK images are acquired simultaneously with ADC maps was established using a restricted diffusion standard phantom [13] and healthy volunteers.

The aim of this study was to determine whether the simple DKI technique using the newly developed software is useful in differentiating head and neck tumors from normal tissue.

Materials and Methods

Patients. This retrospective study enrolled 27 patients, including 12 men and 15 women, with age ranging from 17 to 92 years and a mean age of 68 years, who underwent head and neck MRI for creating ADC maps as part of their routine medical care between March 2019 and September 2021 and were pathologically diagnosed with head and neck malignant tumors. One case of metastatic cancer, ten cases with a tumor diameter of 10 mm or less, and three cases with artifacts on images of the lesion area were excluded. The study protocol was approved by the Ethics Committee of the Okayama University Graduate School of Medicine, Dentistry and Pharmaceutical Sciences and Okayama University Hospital (KEN2011-041). Informed consent was obtained from all patients.

MRI and sequence. The MRI machines used were 3T MAGNETOM Skyra, 3T MAGNETOM Prisma, 3T MAGNETOM Verio, and 1.5T MAGNETOM Aera (Siemens Healthcare, Munich, Germany). MRI was performed using head and neck coils.

Axial DWI was performed with a RESOLVE sequence with STIR for fat suppression [14]. The representative parameters were as follows: repetition time/echo time = 6,990 – 12,300/55 – 84 msec; slice thickness = 3 mm; gap = 4 mm; field of view = 200 × 200 mm; matrix = 140 × 140, 128 × 128, and 126 × 126; bandwidth = 990 Hz/pixel; diffusion mode = 3 scan trace; readout segments = 3; b-value = 0, 400, and 800 sec/mm^2; and direction = 3. A generalized auto-calibrating partially parallel acquisitions (GRAPPA) was set to 2.0 as the parallel imaging reduction factor. The average imaging time for these DW images was 390 (205-769) sec.

In addition to DWI, T1-weighted, T2-weighted short tau inversion recovery (STIR), and contrast-enhanced T1-weighted MRI were performed as part of the routine clinical practice.

Creation of DK images and ADC maps. In this retrospective study, DW images, which were previously taken for ADC maps, were used to create DK images and ADC maps simultaneously using the simple DKI technique.

Images in which the mean kurtosis (MK) values were calculated using DW images at three b-values are hereafter referred to as DK images.

Our software [12] developed for simple DKI created DK images simultaneously with ADC maps using DW images at multiple b-values. This software is based on macro programs of the image analysis software ImageJ (U.S. National Institutes of Health, Bethesda, MD, USA) and Microsoft Excel (2019; Microsoft, Redmond, WA, USA). In each pixel of DW images at b-values of 0, 400, and 800 sec/mm^2, each signal value was logarithmized and plotted on the vertical Y axis, and the b-values were plotted on the horizontal X axis. These values were approximated for the quadratic function $y = Ax^2 + Bx + C$, and then the quadratic coefficient A and linear coefficient B were calculated to obtain the MK value for each pixel using equation (1); the MK value was utilized by ImageJ to create DK images [12].

$$MK = 6A/(-B)^2 \qquad (1)$$

In the ADC map creation, in each pixel of DW images at b-values of 0, 400, and 800 sec/mm^2, each signal value was logarithmized and plotted on the vertical Y axis, and b-values were plotted on the horizontal X axis. These values were approximated for the linear function $y = Ax + B$, and the linear coefficient A was calculated to obtain -A as the ADC value of each pixel; ADC values were utilized by ImageJ for the ADC map.

Region of interest (ROI) settings. ROIs of tumors, hereafter referred to as "tumor ROIs," and normal tissue, hereafter referred to as "normal ROIs," were set as common ROIs in all DW images at b-values of 0, 400, and 800 sec/mm^2.

The ROI was set in the DW image with a b-value of 0 sec/mm^2 in the slice with the largest tumor area according to three radiologists (M.K. with 38 years of experience, J.A. with 25 years of experience, and Y.S. with 5 years of experience) by consensus. T2-weighted STIR MRI was used as a reference to modify the tumor location and shape, when necessary. In addition, the muscles, mainly the masseter muscle, that were clearly depicted in the slice with the largest tumor area were set as normal ROIs (Fig. 1). When the masseter muscle was unclear or out of range, the most clearly defined muscle among the erector spinae, temporalis, and lateral pterygoid muscles was used.

Statistical analysis. For each case, the slice with the largest tumor area was selected, and the MK and ADC values of all pixels in the tumor and normal ROIs in that slice were extracted and analyzed.

Two methods were employed: a pixel analysis, in which all signal values of pixels in the ROI of each case were used, and a median analysis, in which the median signal values of pixels in the ROI of each case were used.

The Shapiro–Wilk test was used to test the normality of data distribution, and the Mann–Whitney *U* test was used to compare the signal values of the tumor and normal ROIs in all DK images and ADC maps. A receiver operating characteristic (ROC) curve analysis was used to evaluate the positive tumor diagnosis rate, and the area under the ROC curve (AUC) and cutoff values were calculated. In the ROC analysis, the test qualities were judged as "excellent," "very good," "good," "satisfactory," and "unsatisfactory" at AUCs of 0.9-1.0, 0.8-0.9, 0.7-0.8, 0.6-0.7, and 0.5-0.6, respectively. The cut-off value was set as the point closest to the upper-left corner.

Spearman's rank correlation test in the pixel analysis was used to determine the relationship between the ADC and MK values at each pixel in the ROI. For the median analysis, a correlation analysis was used to determine the relationship between the median ADC and MK values of each patient. In the correlation analysis, the strengths of association were judged as "perfect," "very strong," "strong," "moderate," "weak," and "absent" at Spearman's rank correlation coefficient (*rs*) values of 0.8-1.0, 0.6-0.8, 0.4-0.6, 0.2-0.4, and 0.0-0.2, respectively.

Statistical analyses were performed using SPSS version 27.0 (IBM Corp., Armonk, NY, USA) and Bell Curve for Excel (Social Survey Research Information Co., Ltd., Tokyo). Statistical significance was set at a p value < 0.05.

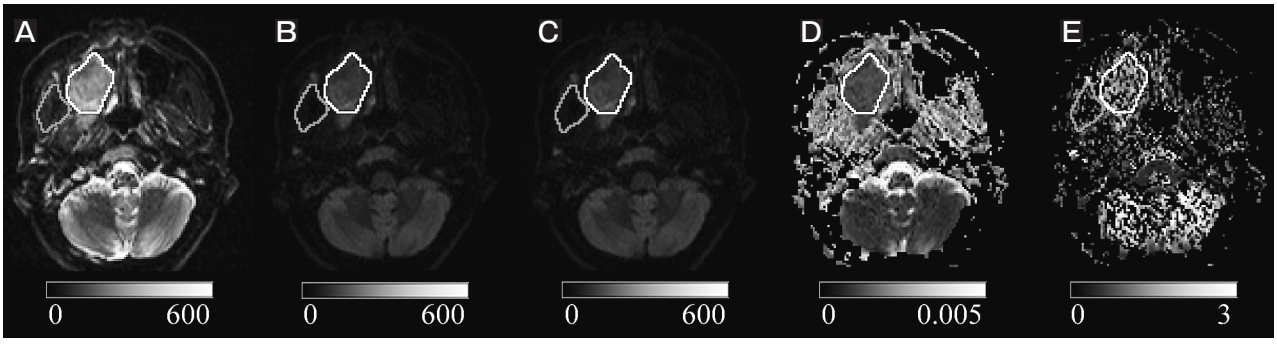

Fig. 1 A DK image and an ADC map created using the same shared DW images. The DW image, ADC map, and DK image of case #9 are shown. (**A**) DW image (b = 0 sec/mm^2), (**B**) DW image (b = 400 sec/mm^2), (**C**) DW image (b = 800 sec/mm^2), (**D**) ADC map, and (**E**) DK image. The white lines indicate the tumor ROIs, and the gray lines indicate the normal ROIs surrounding the right temporalis muscle.

Results

After applying the eligibility criteria, 13 malignant tumors (8 squamous cell carcinomas (SCC), 2 adenoid cystic carcinomas, 1 acinic cell carcinoma, 1 malignant lymphoma, and 1 osteosarcoma) were finally included in this study (Table 1).

The total number of pixels within the ROIs established for each case was 2,579 (mean: 198; median: 172) for the tumor ROIs and 2,141 (mean: 165; median: 177) for the normal ROIs. The number of pixels did not differ significantly between the tumor and normal ROIs in the Mann–Whitney *U* test ($p = 0.762$).

For each case, DK images and ADC maps were simultaneously created from DW images at b-values of 0, 400, and 800 sec/mm^2. Figure 1 shows the images of case #9.

Differences in MK and ADC values between tumor and normal tissues in each case. Table 2 summarizes the significant differences between tumor and normal tissues in MK and ADC values in DK images and ADC maps for each case using tumor and normal ROIs.

Differences in MK and ADC values between tumor and normal tissues based on pixel and median analyses. The MK values in the DK images and ADC values in the ADC map were compared between tumor and normal ROIs. In both the pixel (Fig. 2) and median analyses (Fig. 3), tumor ROIs had significantly higher MK values (Fig. 2A, Fig. 3A; $p < 0.05$) and significantly lower ADC values (Fig. 2B, Fig. 3B; $p < 0.05$) compared to normal ROIs.

Discriminability of MK and ADC values between tumor and normal tissues based on the ROC analysis. In the pixel analysis (Fig. 4A), the AUC of the MK value was 0.639, indicating a "satisfactory" test quality. The AUC of the ADC value was 0.769, indicating a "good" test quality. In the median analysis, the AUC (Fig. 4B) of the MK value was 0.743 and that of the ADC value was 0.746, both of which indicated a "good" test quality.

Relationship between MK and ADC values in the correlation analysis. Figure 5A shows the correlation between the MK and ADC values in the pixel analysis. The MK and ADC values were inversely correlated, with pixels with higher MK values having lower ADC values. The *rs* value was −0.48, indicating a "mod-

Table 1 Case information and the site and number of pixels of the region of interest

Case	Histological classification	ROI setting			
		Tumor ROI*		Normal ROI**	
		Position	Number of pixels	Position	Number of pixels
1	Squamous cell carcinoma	Maxilla	434	Erector spinae muscle	40
2			334	Masseter muscle	119
3			219	Masseter muscle	214
4			132	Lateral pterygoid muscle	100
5		Mandible	63	Masseter muscle	87
6		Tongue	289	Masseter muscle	322
7			172	Masseter muscle	91
8			21	Erector spinae muscle	300
9	Adenoid cystic carcinoma	Palate	412	Temporal muscle	200
10			59	Masseter muscle	177
11	Acinic cell carcinoma	parotid gland	173	Masseter muscle	83
12	Malignant lymphoma	Maxilla	154	Masseter muscle	186
13	Osteosarcoma	Mandible	117	Erector spinae muscle	222

ROI, region of interest.
*ROI of tumor tissue set on the slice showing the maximum area of the tumor.
**ROI of normal tissue set on the erector spinae, masseter, lateral pterygoid, or temporalis muscle on a slice of tumor ROI.

Table 2 Mean kurtosis and apparent diffusion coefficient values for each case

Case	MK value			ADC value		
	Tumor ROI Median (Q1, Q3)	Normal ROI Median (Q1, Q3)	*P*-value	Tumor ROI Median (Q1, Q3) [$\times 10^{-6}$ mm^2/sec]	Normal ROI Median (Q1, Q3) [$\times 10^{-6}$ mm^2/sec]	*P*-value
1	0.67 (0, 1.35)	0.79 (0, 0.99)	0.412	1,219 (1,054, 1,447)	1,765 (1,572, 1,978)	0
2	1.09 (0.3, 1.64)	0.72 (0, 1.06)	0	1,027 (909, 1,198)	1,705 (1,343, 2,213)	0
3	1.36 (0.4, 2)	0.5 (0, 0.91)	0	878 (813, 969)	1,695 (1,457, 2,183)	0
4	1.21 (0.66, 1.53)	1.23 (0.02, 1.71)	0.514	1,179 (956, 1,380)	1,074 (664, 1,477)	0.273
5	0.88 (0.72, 1.08)	1.85 (1.44, 2.28)	0	1,727 (1,580, 2,247)	877 (719, 1,059)	0
6	0.88 (0.59, 1.19)	0.72 (0, 1)	0	1,753 (1,300, 2,185)	2,002 (1,645, 2,465)	0
7	0.82 (0.51, 1.14)	0.67 (0, 0.93)	0.006	1,771 (1,369, 2,121)	2,073 (1,617, 2,630)	0
8	0.32 (0, 1.05)	0.46 (0, 0.94)	0.600	1,733 (1,484, 2,185)	1,934 (1,598, 2,301)	0.302
9	0.91 (0.02, 1.42)	0 (0, 0.78)	0	1,145 (1,014, 1,281)	2,039 (1,669, 2,617)	0
10	0.05 (0, 0.99)	0 (0, 0.95)	0.977	1,289 (1,063, 1,489)	1,776 (1,350, 2,154)	0
11	1.24 (0.74, 1.52)	0.02 (0, 0.86)	0	1,043 (881, 1,215)	1,701 (1,400, 1,983)	0
12	1.18 (0.32, 1.53)	0.39 (0, 1.08)	0	962 (816, 1,175)	1,598 (1,331, 1,951)	0
13	0.95 (0.08, 1.34)	0.61 (0, 1.08)	0.002	1,373 (1,233, 1,542)	1,698 (1,285, 2,240)	0

ROI, region of interest.
p indicates the result of Mann–Whitney *U* test to compare the signal values of the tumor and normal ROIs in each case.

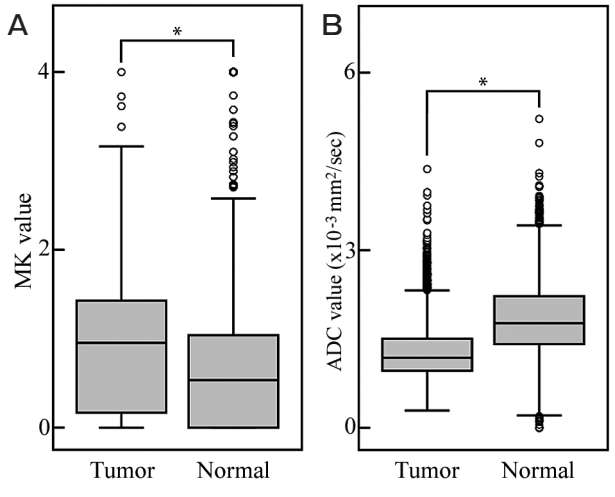

Fig. 2 MK and ADC values of tumor and normal tissues in the pixel analysis. MK (**A**) and ADC (**B**) values for tumor and normal tissues are shown in a box plot of the pixel analysis. Both values differ significantly between the tumor and normal tissues ($p<0.05$).

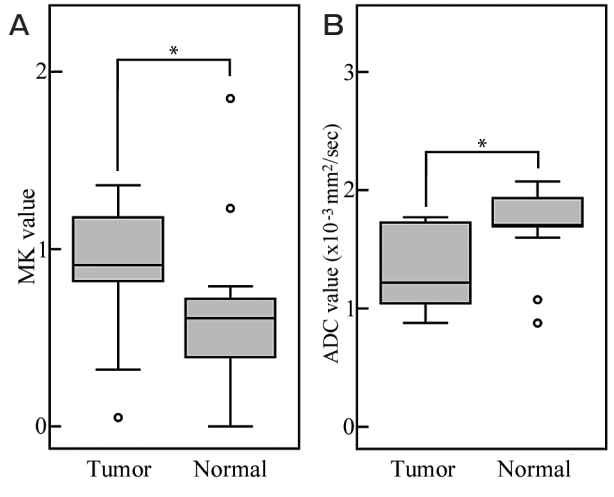

Fig. 3 MK and ADC values of tumor and normal tissues in the median analysis. MK (**A**) and ADC (**B**) values for tumor and normal tissues are shown in a box plot of the median analysis. Both values differ significantly between the tumor and normal tissues ($p<0.05$).

erate" negative association.

Figure 5B shows the correlation between the median MK and ADC values of the tumor and normal ROIs for each case in the median analysis. The MK and ADC values were inversely correlated, with higher MK values having lower ADC values. The *rs* value was –0.67, indicating a "strong" negative association.

Discussion

To the best of our knowledge, this is the first clinical study on this simple DKI technique. Using the new method, DK images were created by using the DW images that are routinely used to create ADC maps in clinical practice. Although the DKI of head and neck tumors has been investigated in clinical dentistry studies, DK images created using this method could contribute to the differentiation of head and neck tumors

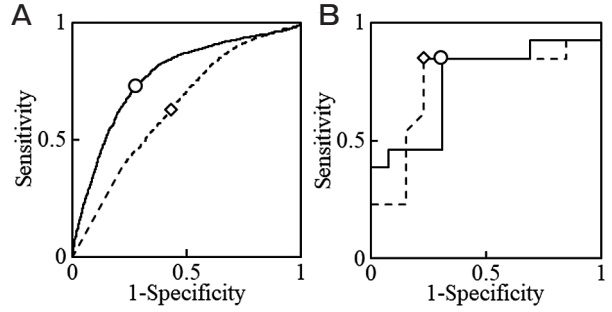

Fig. 4 ROC curve analysis of the ability of MK and ADC values to differentiate tumor and normal tissues. The dotted and solid lines indicate the ROC curves for MK and ADC values, respectively. A diamond (◇) indicates the cutoff MK value, and a circle (○) indicates the cutoff ADC value. (**A**) ROC curve of the pixel analysis. (**B**) ROC curves of the median analysis.

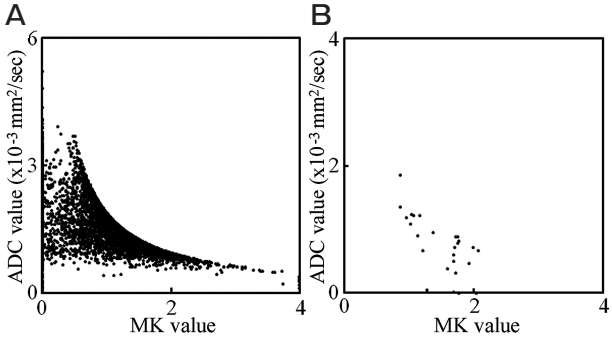

Fig. 5 Correlation analysis between MK and ADC values. (**A**) Scatter plot of the pixel analysis. (**B**) Scatter plot of the median analysis.

from normal tissue in the same way as ADC maps.

Hamada *et al.* [11] reported a method to create RD images using two popular and inexpensive software packages, ImageJ and Excel. Subsequently, Kuroda *et al.* [12] reported a fast DKI method that simultaneously obtained ADC maps and DK images for phantoms and healthy volunteers using three axes and b-values of DWI and the low maximum b-values obtained when creating ADC maps to reduce the imaging time. The aim of our present study was to confirm the usefulness of this technique for simple DKI in differentiating head and neck tumors from normal tissue.

DKI requires imaging in 30 axes, numerous b-values and a high maximum b-value, and these requirements prolong the imaging time. Since dedicated imaging software is not widely available, DKI is not widely used in daily clinical practice [8-10]. In recent years, research has been conducted to reduce the number of axes and b-values in DKI to shorten the imaging time and reduce artifacts caused by body motion, aiming for faster DWI in DKI [15,16]. Regarding the number of axes, many studies have reported the clinical usefulness of DKI in three axes. Since tissues in the head and neck are almost isotropic and have little restricted diffusion, DKI in three axes might be sufficient. Rosenkrantz *et al.* [17] reported that three axes were sufficient for imaging. In three-axis imaging, the smaller the number of b-values, the lesser is the imaging time. Pasicz *et al.* [15] compared seven and four b-values and reported comparable parameters of DKI in healthy participants, indicating the possibility of fast imaging with a reduced number of b-values. In the present study, three axes and b-values were used in DWI to obtain ADC maps for daily practice. The ADC map and DK image could be acquired simultaneously with this single DWI, and the total imaging time for both the ADC map and DK image was 6 min and 30 sec.

For DWI, it is recommended that the maximum b-value be set at 1,000 sec/mm^2 or less when creating ADC maps in daily practice [17]. In our daily clinical practice, a maximum b-value of 800 sec/mm^2 is used to create ADC maps of the head and neck region in dentistry. Although the maximum b-value of 800 sec/mm^2 used to create DK images in this study was low compared to that in previous reports [17] of DKI, Wu *et al.* [18] and Zhang *et al.* [19] reported that DKI at a maximum b-value of 1,400 sec/mm^2 was useful in diagnosing prostate cancer, and Fu *et al.* [20] recently reported that maximum b-values up to 1,000 sec/mm^2 were appropriate for renal cancer.

The novel feature of this simple DKI method is that the ADC map and the DK image are created from the same source images simultaneously in a single DWI; thus, the relationship between the ADC values in the ADC map and the MK values in the DK image can be compared on a pixel-by-pixel basis. This feature allows both to be used simultaneously, and elucidates the characteristics and differences between ADC maps and DK images. Fujima *et al.* [21] reported a similar pixel analysis with an r of −0.42 between ADC and MK values for head and neck SCC. Other authors reported an rs of −0.79 [22] and −0.94 [23] between ADC and MK values for head and neck tumors using ROI-based analysis. Although the correlation between the ADC and MK values in this study was strong, the MK values

varied considerably. In part, this may be because MK values reflect the restricted movement of water molecules in the tumor microenvironment and pathological changes, such as apoptosis and necrosis in the tumor [12, 24], unlike free diffusion expressed as ADC values.

The MK values and maximum b-values in this study were compared with previously reported ones for head and neck tumors. The previously reported MK values for head and neck tumors, which were determined using maximum b-values in the range of 1,500-2,500 sec/mm^2, were approximately 0.87 to 0.92 for SCC, 0.71 to 0.79 for adenoid cystic carcinoma, and 0.82 to 0.92 for malignant melanoma [21-23, 25-27]. For DK images with maximum b-values of 1,000 sec/mm^2 or less, at least four papers have been published [20, 28-30], including those reported in recent years on renal cancer [20, 29, 30], all of which showed good clinical efficacy. In four of these studies, the MK values ranged from 0.62 to 1.84 [20, 28-30], except in the cases of clear cell kidney cancer, which were characterized by low MK values. The median MK values in our present study were approximately 0.91 (mean: 0.89; maximum: 1.36; minimum: 0.05) for all cases and approximately 0.90 (mean: 0.88; maximum: 1.36; minimum; 0.32) for SCC only, and these findings were similar to the previously reported MK values in tumors. Thus the present approach might also be useful for differentiating tumor tissues from normal tissues.

A limitation of this study was the small number of cases. Although significant differences were demonstrated in the median analysis for each case, a selection bias may have been introduced in the cases. Further studies with more cases are needed to improve the reliability of our results. Second, artifacts during DKI may have affected the MK values. Although DW images with obvious artifacts were excluded from the study, unrecognized artifacts may have affected the parameters, and therefore studies on the usefulness and limitations of filter processing to reduce the noise and variability inherent in DKI are required. Third, the low maximum b-value may have affected MK values. In addition, the impact of perfusion might be a subject for future research.

In conclusion, this was the first clinical study on this newly developed simple DKI method. DK images were obtained simultaneously with ADC maps used in daily clinical practice using the inexpensive and widely available software packages ImageJ and Excel, and the created DK images were equally useful in differentiating head and neck tumors from normal tissue when compared to ADC maps.

Acknowledgments. We thank the staff of the Department of Oral Diagnosis and Dentomaxillofacial Radiology, the Department of Radiology, and the Central Department of Radiology, Okayama University Hospital for their support in this study. This study was supported by Grants-in-Aid for Scientific Research (nos. JP22591335, JP15K09924 and JP19K08098) from the Ministry of Health, Labor, and Welfare of Japan.

References

1. Macdonald D, Martin M and Savage K: Maxillofacial lymphomas. Br J Radiol (2021) 94: 20191041. DOI 10.1259/bjr.20191041.
2. Stoia S, Băciuţ G, Lenghel M, Badea M, Băciuţ M, Bran S and Cristian D: Ultrasonography techniques in the preoperative diagnosis of parotid gland tumors–An updated review of the literature. Med Ultrason (2021) 23: 194–202.
3. Jang BG, Huh KH, Kang JH, Kim JH, Yi WJ, Heo MS and Lee SS: Imaging features of chondrosarcoma of the temporomandibular joint: Report of nine cases and literature review. Clin Radiol (2020) 75: 878.e1–e12.
4. Guang ZW, Ling FG, Gui HG, Yao L, Xi ZW and Zhen GY: Magnetic resonance diffusion kurtosis imaging versus diffusion-weighted imaging in evaluating the pathological grade of hepatocellular carcinoma. Cancer Manag Res (2020) 12: 5147–5158.
5. Bhatt AA, Donaldson AM, Olomu OU, Gupta V and Sandhu SJS: Can diffusion-weighted imaging serve as an imaging biomarker for acute bacterial rhinosinusitis? Cureus (2020) 12: 8–12.
6. Jensen JH, Helpern JA, Ramani A, Lu H and Kaczynski K: Diffusional kurtosis imaging: The quantification of non-Gaussian water diffusion by means of magnetic resonance imaging. Magn Reson Med (2005) 53: 1432–1440.
7. Umezawa E, Yoshikawa M, Yamaguchi K, Ueoku S and Tanaka E: Q-space imaging using small magnetic field gradient. Magn Reson Med Sci (2006) 5: 179–189.
8. Wang, J, Dou W, Shi H, He X, Wang H, Ge Y and Cheng H: Diffusion kurtosis imaging in liver: A preliminary reproducibility study in healthy volunteers. Magn Reson Mater Physics Biol Med (2020) 33: 877–883.
9. Jensen JH and Helpern JA: MRI quantification of non-Gaussian water diffusion by kurtosis analysis. NMR Biomed (2010) 23: 698–710.
10. Hui ES, Fieremans E, Jensen JH, Tabesh A, Feng W, Bonilha B, Spampinato MV, Adams R and Helpern JA: Stroke assessment with diffusional kurtosis imaging. Stroke (2012) 43: 2968–2973.
11. Hamada K, Kuroda M, Yoshimura Y, Khasawneh A, Barham M, Tekiki N, Sugianto I, Bamgbose BO, Konishi K, Sugimoto K, Ishizaka H, Kurozumi A, Matsushita T, Ohno S, Kanazawa S and Asaumi J: Evaluation of the imaging process for a novel subtraction method using apparent diffusion coefficient values. Acta Med Okayama (2021) 75: 139–145.
12. Kuroda M, Konishi K, Sugimoto K, Yoshimura Y, Hamada K, Khasawnehc A, Barham M, Tekiki N, Sugianto I, Bamgbose OB, Ishizaka H, Shimizu Y, Nakamitsu Y, Alhammad W, Kamizaki R, Kurozumi A, Matsushita T, Ohno S, Kanazawa S and Asaumi J: Evaluation of fast diffusion kurtosis imaging using new software designed for widespread clinical use. Acta Med Okayama (2022)

76: 297–305.
13. Khasawneh A, Kuroda M, Yoshimura Y, Sugianto I, Bamgbose BO, Hamada K, Barham M, Tekiki N, Konishi K, Sugimoto K, Ishizaka H, Kurozumi A, Matsushita T, Ohno S, Kanazawa S and Asaumi J: Development of a novel phantom using polyethylene glycol for the visualization of restricted diffusion in diffusion kurtosis imaging and apparent diffusion coefficient subtraction method. Biomed Reports (2020) 13: 1–7.
14. Yoshimura Y, Kuroda M, Sugianto I, Bamgbose BO, Miyahara K, Ohmura Y, Kurozumi A, Matsushita T, Ohno S, Kanazawa S and Asaumi J: The usefulness of readout-segmented echo-planar imaging (RESOLVE) for bio-phantom imaging using 3-tesla clinical MRI. Acta Med Okayama (2018) 72: 53–59.
15. Pasicz K, Podgórska J, Jasieniak J, Fabiszewska E, Skrzyński W, Anysz-Grodzicka A, Cieszanowski A, Kukołowicz P and Grabska I: Optimal b-values for diffusion kurtosis imaging of the liver and pancreas in MR examinations. Phys Medica (2019) 66: 119–123.
16. Guan J, Ma X, Geng Y, Qi D, Shen Y, Shen Z, ChenY, Wu E and Wu R: Diffusion kurtosis imaging for detection of early brain changes in parkinson's disease. Front Neurol (2019) 10: 1–6.
17. Rosenkrantz AB, Padhani AR, Chenevert TL, Koh DM, Keyzer FD, Taouli B and Bihan DL: Body diffusion kurtosis imaging: Basic principles, applications, and considerations for clinical practice. J Magn Reson Imaging (2015) 42: 1190–1202.
18. Wu CJ, Zhang YD, Bao ML, Li H, Wang XN, Liu XS and Shi HB: Diffusion kurtosis imaging helps to predict upgrading in biopsy-proven prostate cancer with a Gleason score of 6. Am J Roentgenol (2017) 209: 1081–1087.
19. Zhang YD, Wu CJ, Bao ML, Li H, Yan X, Liu XS and Shi HB: New RESOLVE-based diffusional kurtosis imaging in MRI-visible prostate cancer: Effect of reduced b value on image quality and diagnostic effectiveness. Am J Roentgenol (2016) 207: 330–338.
20. Fu J, Ye J, Zhu W, Wu J, Chen W and Zhu O: Magnetic resonance diffusion kurtosis imaging in differential diagnosis of benign and malignant renal tumors. Cancer Imaging (2021) 21: 1–8.
21. Fujima N, Sakashita T, Homma A, Shimizu Y, Yoshida A, Harada T, Tha KK, Kudo K and Shirato H: Advanced diffusion models in head and neck squamous cell carcinoma patients: Goodness of fit, relationships among diffusion parameters and comparison with dynamic contrast-enhanced perfusion. Magn Reson Imag (2017) 36: 16e23.
22. Minosse S, Marzi S, Piludu F and Vidiri A: Correlation study between DKI and conventional DWI in brain and head and neck tumors. Magn Reson Imag (2017) 42: 114e22.
23. Panyarak W, Chikui T, Tokumori K, Yamashita Y, Kamitani T, Togao O and Yoshiura K: Utility of a diffusion kurtosis model in the differential diagnosis of orofacial tumours. Clin Radiol (2020) 75: 507e519.
24. Yoshimura Y, Kuroda M, Sugianto I, Khasawneh A, Bamgbose BO, Hamada K, Barham M, Tekiki N, Kurozumi A, Matsushita T, Ohno S, Kanazawa S and Asaumi J: Development of a novel method for visualizing restricted diffusion using subtraction of apparent diffusion coefficient values. Mol Med Rep (2019) 20: 2963–2969.
25. Jiang JX, Tang ZH, Zhong YF and Qiang JW: Diffusion kurtosis imaging for differentiating between the benign and malignant sinonasal lesions. J Magn Reson Imaging (2017) 45: 1446–1454.
26. Xiao Z, Tang Z, Qiang J, Qian W, Zhong Y, Wang R, Wang J, Wu L and Tang W: Differentiation of olfactory neuroblastomas from nasal squamous cell carcinomas using MR diffusion kurtosis imaging and dynamic contrast-enhanced MRI. J Magn Reson Imaging (2018) 47: 354–361.
27. Xiao Z, Tang Z, Zheng C, Luo J, Zhao K and Zhang Z: Diffusion kurtosis imaging and intravoxel incoherent motion in differentiating nasal malignancies. Laryngoscope (2020) 130: e727–e735.
28. Quentin M, Pentang G, Schimmöller L, Kott O, Müller-Lutz A, Blondin D, Arsov C, Hiester A, Rabenalt R and Wittsack H: Feasibility of diffusional kurtosis tensor imaging in prostate MRI for the assessment of prostate cancer: Preliminary results. Magn Reson Imaging (2014) 32: 880–885.
29. Zhu Q, Xu Q, Dou W, Zhu W, Wu J, Chen W and Ye J: Diffusion kurtosis imaging features of renal cell carcinoma: A preliminary study. Br J Radiol (2021) 94: 20201374.
30. Zhu J, Luo X, Gao J, Li S, Li S and Chen M: Application of diffusion kurtosis tensor MR imaging in characterization of renal cell carcinomas with different pathological types and grades. Cancer Imaging (2021) 21: 1–9.